Int. J. Electrochem. Sci., 14 **(2019)** 6826 – 6839, doi: 10.20964/2019.07.750

International Journal of
ELECTROCHEMICAL
SCIENCE
www.electrochemsci.org

The Fabrication of Pt/Co Nanocomposite Supported on Reduced Graphene Oxide for Methanol Oxidation

Ying Zhao[1,2*], *Longwei Chen*[1], *Yuedong Meng*[1]

[1] Institute of Plasma Physics, Chinese Academy of Sciences, Hefei 230031, China
[2] University of Science and Technology of China, Hefei 230026, China;
[*]E-mail: zy0808@mail.ustc.edu.cn

Received: 29 March 2019 / *Accepted:* 15 May 2019 / *Published:* 10 June 2019

Cobalt modified Pt-based nanocatalysts supported on reduced graphene oxide (Pt-Co/RGO) was fabricated by a magnetically enhanced inductively coupled plasma (ME-ICP). The analytical results indicated that the objective materials with appropriate particle size, uniform particle distribution, and superior crystal structure were synthesized. The catalytic activity of Pt-based catalyst for methanol oxidation was improved, attributing to the utilization of graphene supports and the metal cobalt. The electrochemically active surface area of Pt-Co/RGO and Pt utilization efficiency is calculated to be 789 $cm^2 \cdot mg^{-1}$ and 69.3%, which is about 6.4 times and 2.88 times higher than the 20 wt.% commercial Pt/C catalyst respectively. The I_f of Pt-Co/RGO is measured to be 410 $mA \cdot mg^{-1}$, which is 4.1 times higher than Pt/RGO and 8 times higher than 20 wt.% Pt/C catalyst. The I_f/I_b ratios of Pt/C, Pt/RGO and Pt-Co/RGO are 1.09, 1.10, and 1.13, respectively. The highest I_f/I_b ratio of Pt-Co/RGO demonstrates that Pt-Co/RGO has a less carbonaceous accumulation and much more tolerance toward CO poisoning.

Keywords: Pt-Co nanocatalyst; methanol oxidation; reduced graphene oxide; magnetically enhanced ICP

1. INTRODUCTION

Direct methanol fuel cell (DMFC) has been widely concerned for its high energy density, mild operation condition, and extensive application areas. Electro-catalyst is the core and foundation of electrochemistry process including energy transformation and reserve *[1-4]*. Generally, the catalysis reaction proceeds on the surface of nanocatalyst. But the intermediate species of methanol oxidation reaction (MOR) such as CO_{ads} absorbed on the surface of the catalyst take the electrocatalysis active site, which declines the catalyst activity and the battery performance *[5,6]*. At present, most investigations of DMFC are focused on the electro-catalyst design and the increase of electrocatalysis activity to avoid CO_{ads} poisoning.

Transition metal with spare *d* molecular orbital and unpaired *d* electron which decreases the activation energy of the complex reaction, via forming various characteristics of the chemisorption bond, is the predominant electrocatalyst. Platinum group metals (PGM) is more active in using as an electrocatalyst. In PGM, the activity of platinum nanocatalyst is irreplaceable and much more effective for DMFC *[7-11]*. However, platinum as noble metal confronted the difficulties due to the high cost and low reservation of DMFC commercialization. The factors like the crystal form, particles size, particles distribution, electronic structure and supporter of electrocatalyst affecting the electrocatalytic performances have been investigated deeply. Adding one or more metallic elements to the noble metal element, which can be considered as alloying material including several microstructures such as random alloy, shell-core structure, dendrite nanowires and surface-modified structure et al, may generate doping effect showing up as surface effect and electronic effect. The shifty surface effect can accelerate the electrocatalytic reaction, and the electronic effect can reduce active energy *[4,12-14]*. Therefore, noble metal alloy can enhance catalytic activity, reduce cost, improve the utilization rate of the noble metal and provide a more applicable and practical way for catalyst commercialization.

Alloying nanocatalyst with the special property of each element and the synergistic effect between heterogeneous atoms can be synthesized in particular composition and microstructure. In order to maximize electronic performance and CO_{ads} poison tolerance of Pt-based nanocatalyst, metals such as Sn, Ru, Cr, Co, Ni, Au, Ag have been proved to behave beneficial improvement of the electrocatalytic property of Pt-based alloying nanocatalyst for MOR by scholars worldwide *[14-17]*. With density functional theory, M. Wakisaka demonstrated that the change in the electronic state of Pt by Co is the key to the high CO tolerance via an XPS system combined with an electrochemical cell (EC-XPS). It was revealed that the Pt/Co alloy resulting in a positive core level shift of Pt could weaken the Pt-CO interaction [18, 19]. The catalyst supports on which the nanocatalyst disperses can restrain the agglomeration of nanoparticles. Graphene oxide (GO) with a large specific surface area can anchor the nanoparticles due to its specific functional group and cellular structure on the surface. GO can avoid being eroded by the electrolyte and noble metal nanoparticles that prevent particles loss and agglomeration [20-26].

Chemical reduction method in aqueous is a common method of metal nanoparticles synthesis. The form and structure of metal nanoparticles are determined by the concentration and the relative proportion of metal precursor and surfactants. Nevertheless, the reduction can also be induced by reductive plasma generated by gas discharge, without any additional chemical reagent. Non-thermal plasmas with high active particles, charged particles, ultraviolet and X-ray provide activation energy and condition for chemical reaction [27-30]. Herein, an efficient cobalt-modified Pt-based nanocatalyst supporting on reduced graphene oxide (Pt-Co/RGO) is synthesized by magnetically enhanced inductive coupling plasma (ME-ICP). Metal nanocatalyst with a certain size, crystal face and structure can be synthesized by optimizing plasma conditions. The electrocatalytic characterization shows that the prepared Pt-based nanocatalyst possesses excellent electrocatalytic activities and stability for MOR.

2. EXPERIMENTAL

2.1. Preparation of stock solution

Pt (IV) stock solution (6 g·L^{-1}) and Co (II) stock solution (3 g·L^{-1}) are prepared separately by dissolving appropriate amounts of analytical reagent grade chloroplatinic acid hexahydrate ($H_2PtCL_6 \cdot 6H_2O$) and cobalt chloride hexahydrate ($CoCL_2 \cdot 6H_2O$) (J&K chemical Co, Beijing, China). Graphene oxide (XF-NANO Materials, Nanjing, China) is synthesized via modified Hummers method. The graphene oxide (100 mg) is dispersed in 100 ml aqua distillate, and use ultrasonic dispersion for 1 h to obtain a uniform GO aqueous solution (1 g·mL^{-1}). The GO stock solution was employed as adsorbents to support active materials and remove them from stock solutions.

2.2. Preparation of Pt-Co/RGO catalysts

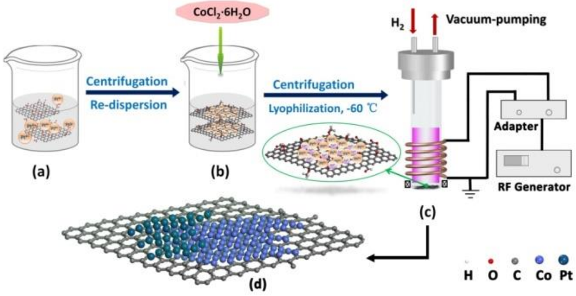

Figure 1. The synthesis process of Pt-Co/RGO.

The fabrication process of Pt-Co/RGO is schematically demonstrated in Fig.1. In order to acquire the objective loading of Pt and Co, the concentration and dosage of each reactant was determined by batch sorption experiment. Firstly, the GO stock solution (1 g·L^{-1}, 75 mL) adjusted to pH≈5 by adding negligible volumes of 0.1 mol/L NaOH is dispersed in the Pt(IV) solution (0.12 g·L^{-1}, 400 mL). The mixture marked as (a) is stirred magnetically for 2 h at a temperature of 333 K and centrifuged at 10000 r·min^{-1} by super centrifuge (Allegra X-15R, BECKMAN, USA). The centrifugate with Pt (IV) can be recycled, and the solid of centrifugation is washed 3 times by aqua distillate, and re-dispersed in 50 ml distilled water to form a new mixture solution marked as (b). The solution (b) is divided into several equal parts for next step. Then Co (II) stock solutions (3 g·L^{-1}) with an appropriate volume were added to the system. Each mixture solution was stirred magnetically for 1 h at a temperature of 333 K and centrifuged at 10000 r·min^{-1}. The centrifugate with Co (II) can be recycled, and the solid of centrifugation is washed 3 times by aqua distillate, and then freeze-dried under vacuum at 213 K. The new solid materials marked as (c) are reduced by ME-ICP H_2 plasma which was generated at discharge power of 100 W, and gas flow rate of 0.6 sccm. The atom ratio of Pt and Co which was loaded on the surface of RGO is calculated by the results of the Pt and Co mass content of the prepared catalyst. The Pt mass content of the Pt/RGO and PtCo/RGO catalysts determined by ICP-MS are 27 wt.% and 17.6 wt.%. The atom ratio of Pt and Co of PtCo/RGO catalyst is calculated to be

1:3. The ME-ICP device is made up of a quartz tube reactor, a 5 windings copper coil, gas supply, vacuum system, and RF power generator. The experimental parameters of the discharge reaction are optimized by batch experiments.

2.3. Measurement of structure and morphology characterization

X-ray diffractometer (X'PertPro MPD, Panalytical, Netherlands) with a Cu Ka radiation ($Cu_{\lambda}K_{\alpha 1}$=0.15418 nm) was used to record the XRD date. The operating condition is 40 kV and 40 mA respectively. X-ray photoelectron spectroscopy (XPS) spectra with an X-ray photoelectron spectrometer (ESCALAB 250, Thermo Fisher, USA) using Al K Alpha source is utilized to determine the elements containing in the prepared catalysts. A transmission electron microscopy (TEM) (JEM-(2010), JEOL, Japan) operated at 100 kV and energy dispersive spectroscopy (EDS) were used to analyze the crystal structure, the morphology, and metal nanoparticles loaded on RGO. The amounts of Pt and Co loaded on RGO are determined by an inductively coupled plasma mass spectrometry (ICP-MS) (iCAP Qc, Thermo Fisher, USA). A microscopes Raman spectrometer (inVia reflex, Renishaw, UK) with a 532 nm argon laser was utilized to record the Raman spectra at room temperature. The function groups conversion of GO after plasma treatment are determined by Fourier Transform Infra-red (FTIR) spectrometer (NEXUS, Thermo Nicolet, USA).

2.4. Electrochemical measurement

Electrochemical workstation (CHI660e, Chenhua, CN) with a standard three-electrode cell was used to carry out the electrochemical test. In the test system, glassy carbon electrode (inner diameter 3 mm) coated with the prepared catalyst was used as working electrode. Pt wire and Ag/AgCl was regarded as counter electrode and reference electrode respectively. The geometric area of the glassy carbon electrode is about 0.07 cm^2. 10 μL of the catalyst ink prepared by dispersing 5 mg of the catalyst powder in a mixture of 0.5 mL ethanol, 0.5 mL distilled water, and 0.2 mL 5 wt.% Nafion solution (DUPONT, USA), is uniformly spread on the surface of the pre-polished glassy carbon electrode, and then dried using an infrared lamp. The processes were repeated at least 5 times [31, 32]. The Pt loading of 0.01 mg for every prepared working electrode is strictly restrained. The curves of hydrogen electro-sorption peaks were recorded in 0.5 M H_2SO_4 solution pre-purified by nitrogen gas with voltage ranging from -0.3 to 1.2 V for about 20 min and a scanning rate about 50 $mV\cdot s^{-1}$. The electrochemically active surface area (ECSA) ($cm^2\cdot mg^{-1}$) of the catalyst is calculated by using the below equation [33]:

$$S_{\mathrm{ECSA}}=\frac{Q_{\mathrm{H}}}{q_{\mathrm{H}}\times m_{\mathrm{Pt}}}$$

Where m_{Pt} and q_{H} are Pt wt.% (mg) and the adsorption charge density of monolayer hydrogen atoms on Pt surface (2.1×10^{-4} $C\cdot cm^{-2}$), respectively. The Coulomb charge Q_{H} (unit in C) for monolayer adsorption of hydrogen is calculated by the integration of hydrogen adsorption area after double-layer correction. The chemical surface area (CSA, $cm^2\cdot mg^{-1}$) is calculated by the following formula:

$$S_{\mathrm{CSA}}=\frac{6}{\rho d}\times 10^{4}$$

Where d is the average size (nm) of Pt particle according to TEM result. The ρ is the density of platinum (21.09 g·cm^{-3}). The effective utilization (η, %) of Pt is calculated from the S_{ECSA} and S_{CSA}.

$$\eta=\frac{S_{\mathrm{ECSA}}}{S_{\mathrm{CSA}}}\times 100\%$$

The activity of MOR occurred in 0.5 M H_2SO_4 and 1 M CH_3OH electrolyte which had been purged by nitrogen, can be characterized by cyclic voltammetry (CV). The operating potential and scan rate was 0~1 V and 50 mV·s^{-1}, respectively. The chronoamperometry was adopted to investigate the stability of the prepared catalysts in 0.5 M H_2SO_4 and 1 M CH_3OH electrolyte with the potential about 0.4 V.

3. RESULTS AND DISCUSSION

3.1. Characterization

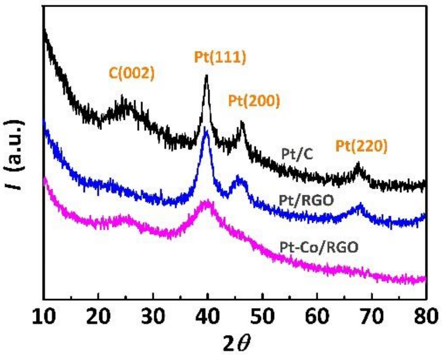

Figure 2. XRD patterns of Pt/C, Pt/RGO and Pt-Co/RGO.

The electrocatalytic performance is determined by the surface structure of the electro-catalyst involved component, valence, morphology, electronic structure, and atomic arrangement. Fig. 2 shows the XRD patterns of Pt/C, Pt/RGO and Pt-Co/RGO. A face-centered cubic structures (FCCs) would be used to index almost all peaks shown in the XRD patterns. The diffraction peaks at 2θ = 39.8°, 46.2° and 67.5°of Pt/RGO and 20 wt.% commercial Pt/C correspond to the Pt (111), Pt (200), and Pt (220) planes of FCC of Pt (JCPDS No. 4–802), respectively [29]. Pt (111) at 2θ = 40.2° of Pt-Co/RGO shows a slightly positive shift and no peak attribute to Co phase. It is demonstrated that the cobalt atoms enter into the platinum to form an alloying structure which causes a lattice distance of the nanoparticles to shrink slightly. It has been revealed that alloying with Co the electronic structures of Pt atoms will result in a positive core level shift which could weaken the Pt-CO interaction. According to Vegard's law, the lattice constant will decrease and the diffraction angle will move forward when the atoms with a small atomic radius enter the crystal lattice with large atomic radius. The decorating effect of heteroatom Co on Pt nanoparticles would attribute to the shift. Pt (111) often observed in the spherical shape has the lowest surface energy for Pt-based catalyst [34]**.** Scherrer formula can calculate the sizes of nanoparticles which are 4.3 nm, 2.8 nm, and 2.2 nm, respectively. The diffraction peak of GO is located at 2θ =11.0°. The peak center is about 22.5° and 25.5° for Pt/RGO and Pt-Co/RGO, respectively. The d-spacing of C plane (0.35 nm) is close to the graphite (0.33 nm). The similarity would imply that the plasma treatment would remove almost all or partially the oxygen-containing functional groups.

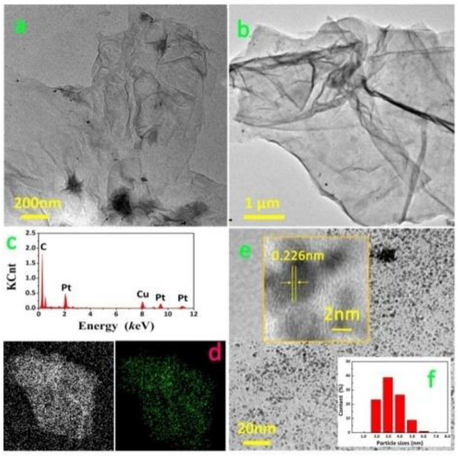

Figure 3. TEM images of (a) GO and (b) Pt/RGO. EDS spectrum (c) of Pt/RGO. EDS elemental mapping (d) of Pt/RGO shows the elements C and Pt. HRTEM image (e) released from Pt/RGO. The inset of (e) is a high-resolution image of a Pt nanoparticle. The image (f) shows the Pt nanoparticle revealing the (111) plane of Pt. The distribution diagram (f) of Pt nanoparticles on the RGO surface.

As shown in Fig.3 (a) and Fig.3 (b), the RGO of Pt/RGO composite maintaining in few layers is similar to the pre-treated GO. Fig. 3 (c) shows that the mass concentration of the Pt supported on RGO calculated by EDS spectrum is about 22 wt.% which is closed to 27.6 wt.% analyzed by MS-ICP. Fig.3 (d) and Fig.3 (e) demonstrate that the Pt NPs distributed on the RGO surface is uniform. The inset of Fig.3 (e) shows a high-resolution image of a Pt nanoparticle. The lattice spacing of the Pt nanoparticle is measured to be 0.226 nm, corresponding to Pt (111) plane of FCC structure. As shown in Fig.3 (f), the sizes of the Pt nanoparticles are evaluated in the range of 2 to 5 nm by using Nano measurer software. Fig.4 (a) shows that the layer of the support RGO is grown due to the addition of cobalt ion which causes the interaction of the individual layer of GO in aqueous. Nevertheless, the distribution of the Pt-Co nanoparticles is still uniform as shown in Fig. 4 (c). Fig.4 (d) shows that the sizes of the Pt-Co nanoparticles are gathered in the range of 2 to 3 nm. Fig.4 (f) inferred that the Pt-Co particles are considered as the single crystalline consisted of the regular arrangement of cobalt and platinum atoms. It could be assumed that the Co particles enter into the Pt cluster which has been supported on GO in advance. It is considered that the element Pt and Co has been formed alloying particles [35-38].

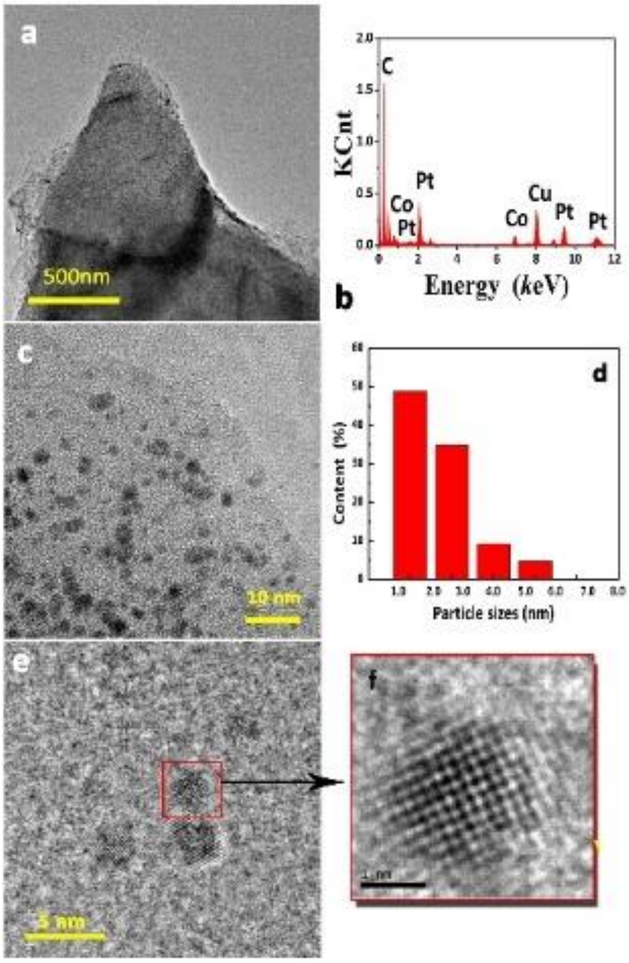

Figure 4. TEM images of (a) Pt-Co/RGO, (b) EDS spectrum of Pt-Co/RGO. HRTEM image (c) and (e) of the Pt-Co/RGO. The distribution diagram (d) of Pt-Co alloying nanoparticles on the RGO surface. The image (f) shows a high-resolution image of single Pt-Co alloying nanoparticle.

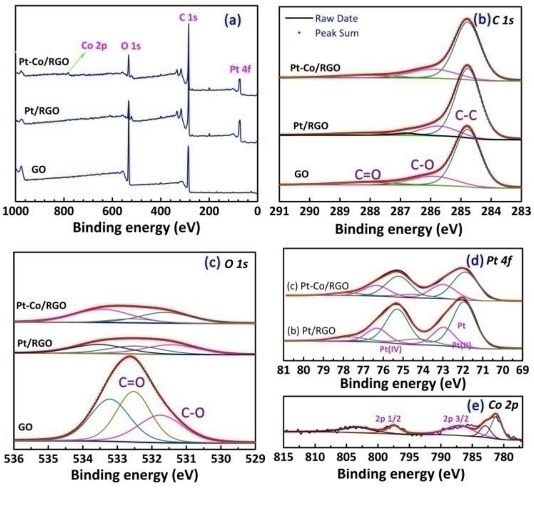

Figure 5. (a) XPS survey spectra of GO, Pt/RGO, and Pt-Co/RGO. XPS core level spectra (b) C 1s, (c) O 1s and (d) Pt 4f of GO, Pt/RGO and Pt-Co/RGO. XPS core level spectra (d) Pt 4f of Pt/RGO and Pt-Co/RGO. XPS core level spectra (e) Co 2p of Pt-Co/RGO.

For qualitative illustration, the surface chemical compositions of GO, Pt/RGO, and Pt-Co/RGO are further performed by the XPS spectra as showed in Fig.5 (a). The C 1*s* XPS core level spectra of several materials are illustrated in Fig.5 (b). According to the C 1*s* spectrum, 4 types of carbon of GO are shown, i.e. C-C (284.6 eV), C-O (286.2 eV), C=O (287.4 eV), and O-C=O (289.1 eV) [39-41]. The C-C peak intensity of Pt/RGO and Pt-Co/RGO is enhanced compared to the peak intensity of GO. In Fig.5 (c), the O 1*s* spectrum of GO shows several types of carbon: C-O (532.5 eV), C=O (531.8 eV) and other oxygenic groups (533.2~533.5 eV). The atomic ratio of intact (C-C) and oxygenated carbon was calculated to be 4.5, which is larger than GO (2.47). The results indicate that oxygenic groups of GO have been partially reduced and removed by ME-ICP plasma. Residual oxygenic groups as active sites are considered to anchor the metal atoms on the surface of RGO. As shown in Fig.5 (d), both of the Pt 4*f* spectrums of Pt/RGO and Pt-Co/RGO have three pairs of peaks. The spin-splitting of Pt $4f_{7/2}$ and Pt $4f_{5/2}$ peaks of Pt/RGO at 70.6 eV and 73.9 eV can be associated with metallic Pt. The weaker peaks at 71.4 eV and 75.1 eV can be assigned to Pt(II) species, e.g. PtO and $Pt(OH)_2$ [38]. The weakest peaks at 74.1 eV and 78.06 eV can be assigned to Pt(IV) species, e.g. PtO_2 and $Pt(OH)_2O$. It is observed that the metallic Pt, which can provide more suitable sites for methanol decomposition than Pt(II) and Pt(IV) species, takes the dominant place of the existent Pt elements. Compared to the Pt/RGO, a positive shift of the metallic Pt peaks and the decreased intensity is observed for Pt-Co/RGO, owing to the addition of cobalt. Fig.5 (e) showed the Co 2*p* XPS spectrum of Pt-Co/RGO. Unapparent peaks of Co $2p_{3/2}$ around 778.48 eV and Co $2p_{3/2}$ at 780.84 eV can be assigned to metallic Co, and Co(II), e.g. $Co(OH)_2$ and CoO, respectively [42].

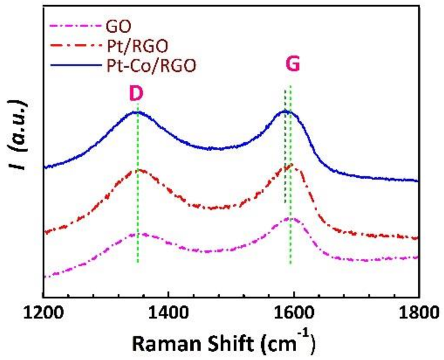

Figure 6. Raman spectra of GO, Pt/RGO, and Pt-Co/RGO.

Raman spectroscopy can be observed in Fig.6 which is a universal method to analysis graphitic materials, the two bands of Raman spectra of GO, Pt/RGO, and Pt-Co/RGO can be assigned to the D and G bands, respectively. The D band of GO, Pt/RGO, and Pt-Co/RGO is almost located at 1351 cm^{-1}, due to the defect structure or partially disordered structures of graphitic domains. G bands are regarded as graphitic carbon. GO has the broader D band at 1351 cm^{-1} and G band at 1598 cm^{-1}. As the metal particles are loaded on the surface of the GO and the reduction reaction occurs, the G bands of Pt/RGO and Pt-Co/RGO shift to around 1590 cm^{-1} and 1585 cm^{-1}, respectively. I_D/I_G for GO is calculated to be 0.72, while that of Pt/RGO and Pt-Co/RGO is calculated to be 0.95 and 1.01, respectively. It showed that the areas oxidized of the GO are partially reduced by ME-ICP plasma, forming small conjugated domains denoted as RGO [43-46].

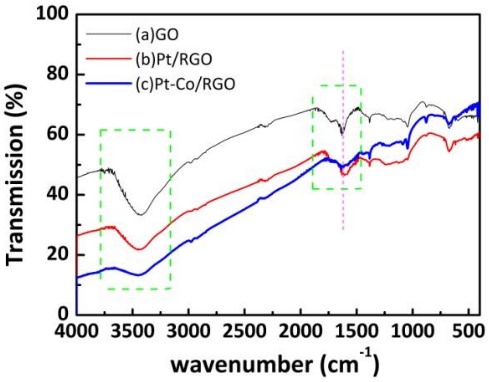

Figure 7. FTIR spectra of GO, Pt/RGO, and Pt-Co/RGO.

Reduction process was investigated via FT-IR spectroscopy. Observed in Fig.7, the broad spectral band centered at near 3455 cm^{-1} is related to the hydroxyl (OH) stretching vibration band. The peak at 1386 cm^{-1} is attributed to the O-H deformation vibration of H_2O due to the inadequacy desiccation. The peak at 1710 cm^{-1} is due to the carbonyl (C=O) stretching vibration of the carboxyl group located on the surface of GO [47]. The peak at 1203 cm^{-1} can be assigned to the C-OH bending vibration band. The peak at 1155 cm^{-1} is considered to be the C-O-C stretching vibration [48]. It is indicated that –OH, -COOH, –C=O and C-O-C are located on the surface of GO. For Pt/RGO and Pt-Co/RGO, O-H stretching vibration band near 3455 cm^{-1} and C=O stretching vibration near 1710 cm^{-1} are decreased apparently owing to the plasma reduction, while the peaks at 1155 cm^{-1} are weakened simultaneously. The results demonstrate that the ME-ICP reduction method is an effective and appropriate method for the reduction of GO supported catalysts, which is highly consistent with the results of Fig.5 (c). It can be observed from Fig.5 (c) that the intensities at C-O (532.5 eV), C=O (531.8 eV) and other oxygenic groups (533.2~533.5 eV) decrease much after plasma reduction. Meanwhile, the metallic Pt and Co were reduced from Pt(II) or Pt(IV) and Co(II) species as illustrated in Fig.5 (d) and (e). The metal nanoparticles (Pt, Pt-Co) attaching to GO can disperse efficiently due to the occupations of the active site and active space on the surface of GO [49, 50].

3.2. Electrochemical characterizations

Cyclic voltammogram is used to measure and compare the electrochemistry performances of the different kinds of catalysts. As shown in Fig.8 (a), the prepared catalysts and 20 wt.% commercial Pt/C electrocatalyst are cycled after 50 cycles in an N_2 saturated 0.5 M H_2SO_4 aqueous solution at a scanning rate of 50 mV·s^{-1} (versus saturated RHE). The ECSA of Pt/C, Pt/RGO and Pt-Co/RGO is calculated to be 124 cm^2·mg^{-1}, 488 cm^2·mg^{-1} and 789 cm^2·mg^{-1}, respectively. The CSA of 20 wt.% Pt/C, Pt/RGO and Pt-Co/RGO are calculated to be 514 cm^2·mg^{-1}, 860 cm^2·mg^{-1} and 1138 cm^2·mg^{-1}, respectively. According to the results, the catalyst Pt-Co/RGO have the largest ECSA of all the prepared catalysts due to the replacement of Pt active sites on the particle surface by Co atoms and smaller size of Pt-Co nanoparticles.

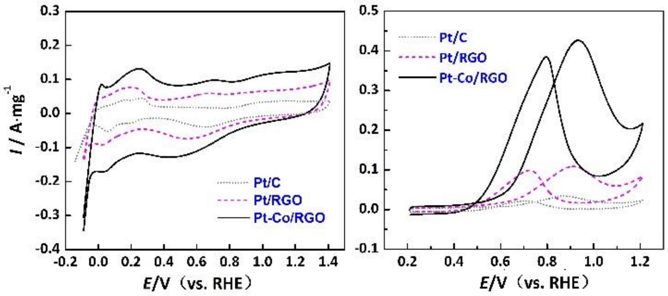

Figure 8. (a) Cyclic voltammogram of Pt/C, Pt/RGO, and Pt-Co/RGO in N_2 saturated 0.5 M H_2SO_4 aqueous solution at a scanning rate of 50 mV/s. (b) Cyclic voltammogram of Pt/C, Pt/RGO and Pt-Co/RGO in N_2 saturated aqueous solution of 0.5 M H_2SO_4 and 1 M CH_3OH mixture, at a scanning rate of 50 mV/s.

The ECSA of Pt-Co/RGO is estimated to be 789 cm^2·mg^{-1} which is about 6.4 times higher than Pt/C catalyst. The Pt utilization efficiency (η, %) for Pt/C, Pt/RGO and Pt-Co/RGO are about 24.10%, 56.73% and 69.30%, respectively. The result indicates that more Pt is available electrochemically for the Pt-Co/RGO catalyst than the other catalysts. It is also demonstrated that the appropriate atom ratio of Pt and Co is importantly related to the electrochemistry performance *[47,51]*. Moreover, the potential of the anode peaks and cathode peaks are very close for Pt-Co/RGO catalyst, indicating a better reversibility for oxidation of methanol on these kinds of catalysts. The double layer current of Pt-Co/RGO is larger than the others, which shows a higher surface effect. The oxygen reduction ability of Pt-Co/RGO catalyst materials is better than Pt-C catalyst, according to nearly potential peaks of anode and cathode in the oxidation area. The cyclic voltammograms of MOR for the prepared catalysts, which are performed in N_2 saturated aqueous solution at a scanning rate of 50 mV/s, are shown in Fig.8 (b). The peak during the forward scan reflects the capacity of methanol oxidation. The current density of the forward scan peak (I_f) for Pt/C (20 wt.%) catalyst is 50 mA·mg^{-1}, as that for the similar loading of Pt/RGO catalyst is 100 mA·mg^{-1}. The I_f value of Pt-Co/RGO is measured to be 410 mA·mg^{-1}, which is 4.1 times higher than Pt/RGO and 8 times higher than 20 wt.% Pt/C catalyst. The current density of the forward scan peak (I_f) for Pt/C (20 wt.%) catalyst is 50 mA·mg^{-1}, as that for the similar loading of Pt/RGO catalyst is 100 mA·mg^{-1}.The I_f of Pt-Co/RGO is measured to be 410 mA·mg^{-1}, which is 4.1 times higher than Pt/RGO and 8 times higher than 20 wt.% Pt/C catalyst. Another peak during the reverse scan is associated with the removal of intermediate carbonaceous species developed in MOR. The ratio of the current density of the two anodic peaks (I_f /I_b) is used to estimate the catalyst tolerance to CO_{ads} accumulated on the electrode surface. With a higher value of I_f/I_b, the poisoning species on the catalyst surface could be removed effectively. The I_f/I_b ratios of Pt/C, Pt/RGO and Pt-Co/RGO are 1.09, 1.10, and 1.13, respectively. It can be found that the I_f/I_b ratio of all are very close and the I_f/I_b ratio of Pt-Co/RGO is the highest among Pt/C, Pt/RGO and Pt-Co/RGO catalysts, implying that Pt-Co/RGO has a less carbonaceous accumulation, and is much more tolerant toward CO poisoning than the others. The results reveal that more active-sites are presented in Pt-Co/RGO catalyst *[52]*. As represented in reference 52, alloying Pt with Co shifts down the d-band center of the larger element. As a result, the strength of the interaction with adsorbates decreases. The Pt-based nanocomposite for methanol oxidation has been reported by a number of authors. The electro-catalysis performances for MOR of several kinds of catalyst from being published literature are compared to the present work in table 1 *[53-56]*. A.K Ghasemi prepared the 3D-HBGP/Pt/Co catalyst using electrodeposition way, of which the ECSA was 203.8 $cm^2 \cdot mg^{-1}$, the Pt and Co nanoparticles average size was 23 nm, and the nanoparticle sizes distribution had a wide range [56]. Comparing to this work, the ECSA of the Pt-Co/RGO according to plasma reduction is obvious higher attributing to the suitable particle sizes and the uniform sizes distribution.

Table 1. Several catalyst's electro-catalysis performances for MOR from works of literature and the present work

S.No	**Catalyst**	**San rate**	**ECSA**	I_f		**Ref.**
		($mv \cdot s^{-1}$)	**($cm^2 \cdot mg^{-1}$)**	**($mA \cdot cm^{-2}$)**	**($mA \cdot mg^{-1}$)**	
1	Pt-Cu/RGO	50	659.8	/	1060	[53]
2	RGO/PtPd	50	230	/	510	[54]
3	Pt@rGO-PANI	50	606	47.2	/	[55]
4	3D-HBGP/Pt/Co	50	203	22.5	/	[56]
5	PtCo/RGO	50	789	65.2	410	Present work

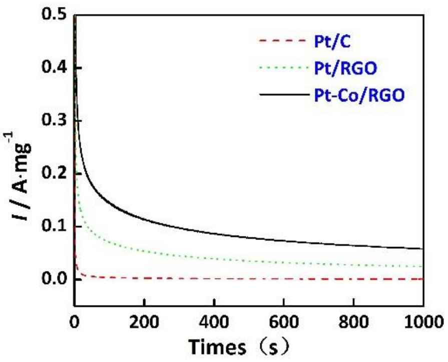

Figure 9. Chronoamperometric curve of Pt/C, Pt/RGO, and Pt-Co/RGO in nitrogen saturated aqueous solution of 0.5 M H_2SO_4 and 1 M CH_3OH mixture at a potential of 0.4 V vs Ag/AgCl (sat.)

As shown in Fig. 9, the electrocatalyst stability of MOR is conducted by chronoamperometry at 0.4 V. It is found that the current per unit of Pt-Co/RGO is the highest of all, implying that the electrocatalytic stability of the Pt-Co/RGO catalyst for MOR is higher than the others. As can be observed from figures 2 and 5, the presence of the metallic Co peaks observed from the XPS data and the absence of the Co peaks in XRD patterns could demonstrate conjunctly the formation of Pt-Co alloys because no peak attributable to Co phase can be observed in the patterns when the Co enters into the Pt lattice to form the Co core Pt shell structure [18, 47]. Attributing to add the second metal cobalt with a certain ratio, the Pt-Co/RGO catalyst shows an improved CO tolerance *[57]*. The second metal is more easily to occur an oxidation reaction than platinum. The oxidation rate of intermediate products produced by MOR is enhanced due to the surface reaction. Meanwhile, the formation of intermediate products which should be strongly absorbed on Pt is suppressed according to the addition of the second metal cobalt. Also, the electronic properties and the surface morphology of Pt are changed due to the existence of the second metal cobalt. The catalyst supported on RGO shows a better stability, on account of the graphene sheets providing the amount of oxygen groups to reinforce the interaction with Pt nanoparticles.

4. CONCLUSION

An ME-ICP device was adopted to fabricate a cobalt-modified Pt-based nanocatalyst supported on reduced graphene oxide. The Pt and Co random alloy structure of Pt-Co/RGO fabricated via this way was certified by XRD and TEM. Due to the introduction of cobalt atom, the Pt nanoparticles lattice structure and the surface morphology were modified and the electronic characteristic was enhanced. It was verified that the oxygen functional groups on GO were feasibly reduced by ME-ICP reduction, and the alloy nanoparticles were attached to the graphene by XPS, Raman and FTIR analysis. The catalytic activity for MOR of Pt-based catalyst was improved attributing to the utilization of graphene supports and the second metal cobalt reasonably. Catalytic reaction sites with proper sizes were well dispersed on the graphene sheets attributing to the characteristic of graphene. As a transition metal, cobalt can adjust d band center of platinum by forming Pt-Co alloy nanoparticles. The present investigations demonstrated that the ME-ICP is an effective approach to fabricate Pt-Co/RGO catalysts. It is found that the I_f/I_b of the prepared Pt-Co/RGO catalyst is the highest among Pt/C, Pt/RGO and Pt-Co/RGO catalysts, which implies that the prepared Pt-Co/RGO has a less carbonaceous accumulation and a much more tolerance toward CO poisoning than Pt/RGO catalysts and commercial Pt/C catalysts.

ACKNOWLEDGMENT
The project is supported by National Natural Science Foundation of China under Grant Nos. 11575252, 11775270, and Natural Science Foundation of Anhui Province under Grant No. 1708085MA26.

References

1. S. K. Kamarudin, F. Achmad, W. R. W. Daud, *Int. J. Hydrogen Energ*y, 34 (2009) 6902-6916.
2. B. C. Ong, S.K. Kamarudin, S. Basri, *Inter. J. Hydrogen Energ*y, 42 (2017) 10142-10157.
3. S. Basri, S.K. Kamarudin, W.R.W. Daud, Z. Yaakub, *Inter. J. Hydrogen Energ*y, 35 (2010) 7957-7970.
4. S. Basri, S.K. Kamarudin, W.R.W. Daud, Z. Yaakob, A.A.H. Kadhum, *Sci. World J.*, 1(2014). 547604.
5. J. Li, F. Li, S.X. Guo, J. Zhang, J.T. Ma, *ACS Appl. Mater. Inter.*, 9 (2017) 8151-8160.

6. X. Q. Shi, Y. Wen, X. Y. Guo, Y. X. Pan, Y. Y. Ying, Y. Ying, H. F. Yang, *Acs Appl. Mater. Inter.*, 9 (2017) 25995-26000.
7. J. K. Norskov, J. Rossmeisl, A. Logadottir, L. Lindqvist, J.R. Kitchin, T. Bligaard, H. Jonsson, *J. Phys. Chem*. B, 108 (2004) 17886-17892.
8. B. Beden, C. Lamy, J.M. Leger, *J. Electroanal. Chem*., 101 (1979) 127-131.
9. J. Greeley, T. F. Jaramillo, J. Bonde, I. B. Chorkendorff, J. K. Norskov, *Nat. Mater*., 5 (2006) 909-913.
10. K. L. Nagashree, M. F. Ahmed, *Synthetic. Met*., 158 (2008) 610-616.
11. S. M. Paek, E. Yoo, I. Honma, *Nano. Lett*., 9 (2009) 72-75.
12. M. Rashid, T. S. Jun, Y. Jung, Y. S. Kim, *Sensor. Actuat B-Chem*., 208 (2015) 7-13.
13. Y. Liu, M. F. Chi, V. Mazumder, K. L. More, S. Soled, J. D. Henao, S. H. Sun, *Chem. Mater*., 23 (2011) 4199-4203.
14. M. V. Martinez-Huerta, J. L. Rodriguez, N. Tsiouvaras, M. A. Pena, J. L. G. Fierro, E. Pastor, *Chem. Mater*., 20 (2008) 4249-4259.
15. H. Wang, Q. P. Zhao, Q. Ma, *Ionics*, 21 (2015) 1703-1709.
16. X. L. Sui, Z. B. Wang, C. Z. Li, J. J. Zhang, L. Zhao, D. M. Gu, S. Gu, *J Mater. Chem*. A, 3 (2015) 840-846.
17. C. T. Hsieh, J. Y. Lin, *J. Power. Sources*, 188 (2009) 347-352.
18. M. Wakisaka, S. Mitsui, Y. Hirose, K. Kawashima, H. Uchida, and M. Watanabe, *J. Phys. Chem*. B, 110 (2006) 23489-23496.
19. P. H. Fernandez, M. Montiel, P. Ocon, J. L. G. Fierro, H. Wang, H. D. Abruna, S. Rojas, *J. Power Sources*, 195 (2010) 7959-7967.
20. T. F. Li, Y. X. Peng, K. Li, R. Zhang, L. R. Zheng, D. G. Xia, X. Zuo, *J. Power Sources*. 293 (2015) 511-518.
21. K. Kakaei, H. Gharibi, *Energy*, 65 (2014) 166-171.
22. R. Kou, Y. Y. Shao, D. H. Wang, M. H. Engelhard, J. H. Kwak, J. Wang, V. V. Viswanathan, C. M. Wang, Y. H. Lin, Y. Wang, I. A. Aksay, J. Liu, *Electrochem. Commun*., 11 (2009) 954-957.
23. Y. M. Li, L. H. Tang, J. H. Li, *Electrochem. Commun*., 11 (2009) 846-849.
24. Y. M. Tan, C. F. Xu, G. X. Chen, N. F. Zheng, Q. J. Xie, *Energ. Environ. Sci*., 5 (2012) 6923-6927.
25. X. L. Wang, C. Li, G. Q. Shi, *Phys. Chem. Chem. Phys*., 16 (2014) 10142-10148.
26. Q. Wang, Z. L. Zhao, Y. L. Jia, M. P. Wang, W. H. Qi, Y. Pang, J. Yi, Y. F. Zhang, Z. Li, Z. Zhang, *Acs Appl. Mater. Inter.*, 9 (2017) 36817-36827.
27. E. T. Thostenson, Z. F. Ren, T. W. Chou, *Compos. Sci. Technol.*, 61 (2001) 1899-1912.
28. S. Iijima, Helical Microtubules of Graphitic Carbon, *Nature*, 354 (1991) 56-58.
29. Z. F. Ren, Z. P. Huang, J. W. Xu, J. H. Wang, P. Bush, M. P. Siegal, P. N. Provencio, *Science.*, 282 (1998) 1105-1107.
30. R. Chetty, S. Kundu, W. Xia, M. Bron, W. Schuhmann, V. Chirila, W. Brandl, T. Reinecke, M. Muhler, *Electrochim. Acta.*, 54 (2009) 4208-4215.
31. R. P. Antony, L. K. Preethi, B. Gupta, T. Mathews, S. Dash, A. K. Tyagi, *Mater. Res. Bull*. 70 (2015) 60-67.
32. J. Ma, L. Wang, X. Mu, Y. Cao, *J. Colloid. Interf. Sci*., 457 (2015) 102-107.
33. H. A. Gasteiger, N. M. Markovic, P. N. Ross, *J. Phys. Chem*., 99 (1995) 16757-16767.
34. T. H. M. Housmans, A. H. Wonders, M. T. M. Koper, *J. Phys. Chem.* B., 110 (2006) 10021-10031.
35. Y. Hou, Z. H. Wen, S. M. Cui, S. Q. Ci, S. Mao, J. H. Chen, *Adv. Funct. Mater*., 25 (2015) 872-882.
36. Z. S. Wu, L. Chen, J. Z. Liu, K. Parvez, H. W. Liang, J. Shu, H. Sachdev, R. Graf, X. L. Feng, K. Mullen, *Adv. Mater*., 26 (2014) 1450-1455.
37. J. R. Kitchin, J. K. Norskov, M. A. Barteau, J. G. Chen, *J. Chem. Phys*., 120 (2004) 10240-10246.
38. Y. J. Hu, P. Wu, Y. J. Yin, H. Zhang, C. X. Cai, *Appl. Catal. B-Environ*., 111 (2012) 208-217.
39. C. Shan, H. Yang, J. Song, D. Han, A. Ivaska, L. Niu, *Anal. Chem*., 81 (2009) 2378-2382.

40. G. P. Lopez, D. G. Castner, and B. D. Ratner, *Surf. and Interf. Analys*., 17 (1991) 267-272.
41. M. Wu, Q. Feng, X. Sun, H. Wang, G. Gielen, W. Wu, *Sci. Rep*., 5 (2015) 10001.
42. L. Yi, L. Liu, X. Liu, X. Wang, W. Yi, P. He, X. Wang, *Inter. J. Hydrogen Energ*., 37 (2012) 12650-12658.
43. M. M. Shahid, P. Rameshkumar, A. Pandikumar, H. N. Lim, Y. H. Ng, N. M. Huang, *J. Mater. Chem.* A., 3 (2015) 14458-14468.
44. F. Tuinstra, J. L. Koenig, *J. Chem. Phys*., 53 (1970) 1126-&.
45. H. Kim, D. H. Seo, S. W. Kim, J. Kim, K. Kang, *Carbon*, 49 (2011) 326-332.
46. Y. J. Zhang, T. Mori, L. Niu, J. H. Ye, Energ. *Environ. Sci.*, 4 (2011) 4517-4521.
47. M. M. Zhang, Y. Li, Z.X. Yan, J. J. Jing, J. M. Xie, M. Chen, *Electrochim Acta*., 158 (2015) 81-88.
48. H. Dai, C. Yang, X. Ma, Y. Lin, G. Chen, *Chem. Commun*., 47 (2011) 11915-11917
49. K. P. Liu, J.J. Zhang, G.H. Yang, C.M. Wang, J.J. Zhu, *Electrochem. Commun*., 12 (2010) 402-405.
50. Y. Si, E.T. Samulski, *Nano Lett.*, 8 (2008) 1679-1682.
51. R. Chetty, W. Xia, S. Kundu, M. Bron, T. Reinecke, W. Schuhmann, M. Muhler, *Langmuir*, 25 (2009) 3853-3860.
52. P. Yu, M. Pemberton, P. Plasse, *J. Power Sources*., 144 (2005) 11-20.
53. F. Li, Y. Guo, M. Chen, H. Qiu, X. Sun, W. Wang, Y. Liu, J. Gao, *Int. J. Hydrogen Energy*, 38(2013) 14242-249.
54. S.F. Du, Y.X. Lu, R.S. Wilckens, *Carbon*, 79(2014) 346-53.
55. S. Eris, Z. Dasdelen, Y. Yıldız, F. Sen, Int. *J. Hydrogen Energ*., 43(2018) 1337-43,
56. A.K. Ghasemi, M Ghorbani., M.S. Lashkenari, S.R. Shabanian, *J. Taiwan Inst. Chem*. E., 91(2018) 345-57.
57. V. R. Stamenkovic, M. Arenz, C. A. Lucas, M. E. Gallagher, P. N. Ross, N. M. Markovic, *J. Am. Chem. Soc*., 125 (2003) 2736-2745.